N-, O- and P-doped hollow carbons: Metal-free bifunctional electrocatalysts for hydrogen evolution and oxygen reduction reactions

Senchuan Huang, Yuying Meng[*], Yangfei Cao, Shiman He, Xiaohui Li, Shengfu Tong, Mingmei Wu[*]

MOE Key Laboratory of Bioinorganic and Synthetic Chemistry, School of Chemistry, Sun Yat-Sen University, No. 135, Xingang Xi Road, Guangzhou 510275, PR China

ARTICLE INFO

ABSTRACT

To realize clean and renewable energy conversion systems, such as fuel cells and water splitting devices, cost-effective and energy-efficient bifunctional metal-free electrocatalysts are highly needed. Herein, N-, O- and P-doped hollow carbons (NOPHCs) are successfully synthesized *via* pyrolysis of Co_2P-containing polypyrrole (Co_2P@PPY) precursors and removal of Co_2P templates. The materials are proven to serve as efficient and stable metal-free bifunctional electrocatalysts toward hydrogen evolution reaction (HER) and oxygen reduction reaction (ORR) in basic media. Notably, $NOPHC_{10}$-900, which is obtained using 0.10 g of Co_2P as template and pyrolyzed at 900 °C, exhibits high electrocatalytic performance for HER with a small overpotential of 290 mV at $-10\,mA\,cm^{-2}$, a low Tafel slope of 102 mV dec^{-1}, and a great long-term stability for 19 h. Moreover, it affords decent electrocatalytic performance for ORR, with positive onset potential, high electron-transfer number, good methanol crossover tolerance and outstanding durability. The excellent electrocatalytic performance is mainly due to the synergistic effect of the multi-heteroatoms dopants in it and the large density of active sites on the surface of the hollow carbons.

1. Introduction

In light of the increasing demand of energy worldwide, the over-consumption of limited fossil fuel reserves and the negative environmental impacts posed by fossil fuels, finding energy materials and systems that can harness renewable sources and provide clean energy has become one of the "holy grails" for researchers [1,2]. Dihydrogen (H_2), which contains the highest gravimetric energy density, has long been recognized as one of the most promising green energy carriers to reduce or eliminate our reliance on fossil fuels. Electrochemical water splitting is an environmentally friendly energy conversion process, which produces H_2 fuel using electricity from renewable sources (*e.g.*, sunlight and wind) [3]. However, this viable and sustainable H_2 generation process still remains elusive and highly challenging, because of the high cost and scarcity of noble metal-based catalysts (*e.g.*, platinum) which are commonly used to lower activation energy barrier of the sluggish half reaction of hydrogen evolution reaction (HER) [4,5]. Therefore, it is of great interest to develop sustainable and highly efficient alternative non-noble metal HER catalysts that are composed of inexpensive and earth-abundant elements.

Over the last decades, tremendous efforts have been devoted to developing highly active and cost-effective electrocatalysts for HER, such as transition metal-based sulfides [6–8], borides [9,10], carbides [11–13], selenides [14], nitrides [15–17], phosphides [18–20], *etc.* However, these HER electrocatalysts suffer from oxidation, leaching, sintering, and/or agglomeration, and as a result, lose their catalytic activity and shelf-life over time during their use [21]. Over the past few years, carbon-based materials have become highly attractive for HER electrocatalysis owing to their excellent electronic conductivity, robust chemical and thermal stability, and environmental friendliness. They can also be coupled with metals or encapsulate metals to form hybrid materials that can electrocatalyze HER [22,23]. In some of such materials, the carbon helps as a good electron transfer, and in other cases it plays a synergistic role with the embedded or supported metals, leading to a remarkable performance in catalyzing HER [24,25].

Heteroatom-doped carbon materials, some of whose carbon atoms in the graphitic structure are replaced by N, O, P and S dopants, can serve as metal-free electrocatalysts with excellent activity and durability for various electrochemical reactions. Heteroatom-doping, especially co- or/and tri-doping, can effectively modulate the electronic structure of the neighboring carbon atoms and decrease the work function of the carbon materials, and thereby boost their

electrocatalytic performances [26]. This was first shown with electrochemical measurements and theoretical calculations for N- and P-dual-doped graphene, which was found to efficiently electrolyze HER [27]. In another work, Chen et al. reported N- and S-co-doping in graphene created a highly electrocatalytically active material for HER in acidic media, and the improved catalytic performance was attributed to the synergistic effects by N-dopant and S-dopant moieties in the material [28]. Besides HER, heteroatom-doped carbon materials have been found to effectively electrolyze oxygen reduction reaction (ORR), the sluggish cathodic reaction in the fuel cells or metal-air batteries. Dai's group developed vertically aligned N-doped carbon nanotubes, which were found to display remarkable ORR catalytic performance and long-term operational stability [29].

Meanwhile, increasing the surface area of the materials by introducing hollow or optimized porous structures in them can create more exposed electrochemically active sites and higher mass transport compared with those in the corresponding bulk materials [30]. So, it is no wonder that there have been lots of research works exploring the design and synthesis of various hollow materials as a way to realize favorable catalytic properties in such materials for applications in electrocatalysis.

Inspired by these previous works, herein we report the synthesis of N-, O- and P-doped hollow carbons (named as NOPHCs) with the assistance of Co_2P nanoparticles, which were used both as the source of P dopant atoms and the sacrificial templates for hollow structures. Interconnected hollow structures, due to the removal of Co_2P nanoparticles, were formed uniformly throughout the heteroatoms-doped carbon materials. Besides, N, O and P dopants homogeneously distributed throughout the graphitic carbon shells. Thanks to the synergistic effect of the multi-heteroatoms doping and the large density of active sites on the surfaces of the materials, NOPHCs showed very good electrocatalytic performance toward both HER and ORR in alkaline media with excellent durability.

2. Experimental section

2.1. Chemical and reagents

Ammonium persulfate $((NH_4)_2S_2O_8)$, pyrrole, potassium hydroxide (KOH), cobalt(II) chloride hexahydrate $(CoCl_2 \cdot 6H_2O)$, sodium hypophosphite (NaH_2PO_2), hydrochloric acid (HCl), sodium thiocyanate (NaSCN), isopropanol and absolute ethanol were obtained from Aladdin. Pt/C (20 *wt*. %) and Nafion solution (5 *wt*. %) were purchased from Johnson Matthey and Sigma-Aldrich, respectively. All the chemical reagents were analytical grade and used as received without further treatment. Deionized water was employed throughout the experiments.

2.2. Synthesis of N-, O- and P-doped hollow carbons (NOPHCs)

Co_2P-containing polypyrrole (Co_2P@PPY) precursor was synthesized using a procedure we reported previously (for more detailed procedure, see Supporting Information, SI) [31,32]. The precursor was placed in a temperature-programmable tube furnace under argon, which was purged with a flow rate of $\sim 30 \, mL \, min^{-1}$, and pyrolyzed at different temperatures: 700, 800, 900, or 1000 °C, in order to carbonize the PPY in the Co_2P@PPY materials. In each case, the furnace temperature was first raised from room temperature to 300 °C at a ramp of $1 °C \, min^{-1}$ and held at 300 °C for 3 h to allow the conversion of amorphous carbon from polymer precursor. Then, the temperature was increased to the final temperature (*i.e.* 700, 800, 900, or 1000 °C) at a rate of $10 °C \, min^{-1}$ and kept at this temperature for 2 h. Finally, the furnace was cooled down to room temperature naturally. These procedures led to Co_2P-containing carbon composite material, named as Co_2P@NOPC.

The Co_2P were removed to form hollow structures within the carbon

material as follows. First, 50 mg of the as-obtained Co_2P@NOPC composite materials synthesized at different final pyrolysis temperatures were dispersed in and stirred with 1.0 M HCl solution (10 mL) at room temperature for 24 h. The dispersions were centrifuged, and black solid products were obtained. They were thoroughly washed with distilled water and dried at 60 °C in oven overnight, and different N-, O- and P-doped hollow carbons (labeled as $NOPHC_{10}$-T), where T represents the final pyrolysis temperature, namely 700, 800, 900 and 1000 °C, were obtained.

In order to investigate the effect of surface area on the materials' electrocatalytic performance, two additional $NOPHC_x$-900 materials were obtained by changing the amount of Co_2P (0.05 and 0.15 g) used as sacrificial template, giving $NOPHC_5$-900 and $NOPHC_{15}$-900, respectively. Moreover, a series of $NOPHC_{10}$-H_t ($NOPHC_{10}$-H_{12} $NOPHC_{10}$-H_{24} and $NOPHC_{10}$-H_{48}) materials was synthesized by tuning the treatment time of the materials in acidic solution (12, 24 and 48 h). In addition, two control materials, namely N-, O- and P-doped carbon black (NOPCB) and N- and O-codoped carbon black (NOCB), were also prepared without the assistance of Co_2P template (see details in SI). The synthetic parameters of all the NOPHCs and the two control samples were compiled in Table S1.

2.3. Electrochemical measurements

2.3.1. Electrocatalytic hydrogen evolution reaction (HER)

The electrochemical and electrocatalytic properties of all the hollow carbons and the control materials were systemically evaluated with a Metrohm Auto Lab (PGSTAT302 N) potentiostat using a traditional three-electrode setup in 1.0 M KOH solution at room temperature. In the typical cell configuration, a saturated Ag/AgCl electrode was used as the reference electrode, a graphite rod with a diameter of 5 mm was used as the counter electrode, and a glassy carbon electrode (GCE) coated with electrocatalysts was used as the working electrode. The values of the potentials, which were experimentally measured with the reference electrode Ag/AgCl electrode, was calibrated and converted to values with respect to reversible hydrogen electrode (RHE) according to the Nernst equation:

$$E \, (V \, vs. \, RHE) = E \, (V \, vs. \, Ag/AgCl) + 0.197 + 0.059*pH$$

The working electrode was prepared according to the following procedures: 1) 2 mg of the prepared electrocatalyst was dispersed in 200 μL of 2-propanol with sonication treatment at least for 30 min or until a homogenous mixture or ink was formed; 2) using a micropipette, 2 μL of the resulting suspension was drop-casted on top of a freshly polished GCE with diameter of 3 mm (loading $\sim 0.28 \, mg \, cm^{-2}$), and it was dried in air; 3) 2 μL of Nafion (0.5 % in 2-propanol) solution was casted onto the top of the electrode and allowed to completely dry under ambient conditions; this was done to protect the electrocatalyst film from falling off.

Prior to each electrocatalytic experiment, the electrolyte was degassed by bubbling N_2 for 30 min. Then, 20 cycles of cycling voltammograms (CVs) were run in a potential window of 0 to -0.6 V *vs.* RHE at a scan rate of $100 \, mV \, s^{-1}$ to activate the electrocatalyst and to reach a steady state. After this, linear sweep voltammograms (LSV) for HER in a potential range of 0 to -0.6 V at a sweep rate of $5 \, mV \, s^{-1}$ were acquired in N_2-saturated 1.0 M KOH solution. Tafel slopes were then obtained from the corresponding polarization curves using the Tafel formula. Chronoamperometry curve was recorded over $NOPHC_{10}$-900 under a constant working potential of -0.29 V for 19 h to evaluate the stability of the material under the electrocatalytic conditions. At the end of the stability test, LSV curve was also acquired. For a comparison, the electrocatalytic performance of commercially available Pt/C (20 *wt*. %) for HER was measured under otherwise identical conditions. More experimental details on the methods and calculations used to obtain the Faradic efficiency, electrochemical impedance spectra (EIS) and

electrochemical surface area (ECSA) were provided in SI.

2.3.2. Electrocatalytic oxygen reduction reaction (ORR)

The oxygen reduction reaction (ORR) was evaluated with a Pine Bipotentiostat (Pine Research Instrumentation) using a conventional three-electrode cell, containing a saturated Ag/AgCl as the reference electrode, a graphite rod as the counter electrode, and a rotating disk electrode (RDE, with a diameter of 5.0 mm) with the catalysts as the working electrode. CVs of variable electrocatalysts were obtained in either O_2- or N_2-saturated 0.1 M KOH solution at a scan rate of 100 mV s^{-1}. LSV curves were acquired on a RDE by scanning the potential from +1.16 to +0.26 V (*vs.* RHE) in O_2-saturated 0.1 M KOH solution at a sweep rate of 2 mV s^{-1} under different rotating speeds (400, 625, 900, 1225, 1600 and 2025 rpm). For fabrication of the working electrode, 8 µL of the electrocatalyst suspension with the concentration of 10 mg mL^{-1} in 2-propanol, prepared earlier for HER, was casted onto the surface of a freshly polished RDE (loading ~0.407 mg cm^{-2}) and dried under atmospheric conditions. After that, the electrode was covered with 4 µL of Nafion (0.5 *wt.* %) solution by drop-casting and dried at room temperature to form a protective film around the catalyst. For comparison, commercially available Pt/C (20 *wt.* %) electrode was used. The procedures used to obtain the electron transfer number (n) associated with the yield of H_2O and hydrogen peroxide (% H_2O_2) byproduct and to perform the methanol crossover test were provided in SI.

3. Results and discussion

3.1. Material characterizations

As illustrated in Fig. 1, NOPHCs were synthesized by a template-assisted pyrolysis method, which involved the synthesis of a solid $Co_2P@PPY$ precursor, the treatment of the precursor at high temperatures, and finally the etching of the carbonized composite product ($Co_2P@NOPC$) in concentrated HCl solution to remove the Co_2P template. Co_2P nanoparticles were synthesized simply by low-temperature treatment of $CoCl_2$ and NaH_2PO_2 (Fig. S1a) and they were used both as sources of P dopant atoms and sacrificial templates to create hollow structures later on. They were then mixed with pyrrole, which was polymerized around the Co_2P nanoparticles using $(NH_4)_2S_2O_8$ as an initiator. Carbonization of the resulting $Co_2P@PPY$ at high temperatures (*i.e.*, 700, 800, 900 and 1000 °C) under inert atmosphere (Ar) and finally, etching of the Co_2P nanoparticles from the carbonized products with HCl solution, resulted in the NOPHCs. By varying the pyrolysis temperature, the relative amount of Co_2P nanoparticles in the precursor, and the etching time with HCl solution, three different series of NOPHC materials were obtained, as shown in Table S1, which were named as NOPHC$_{10}$-T (T = 700, 800, 900 and 1000), NOPHC$_x$-900 (x = 5, 10 and 15), and NOPHC$_{10}$-H$_t$ (H$_t$ = H$_{12}$, H$_{24}$, H$_{48}$), respectively. Here, we denoted NOPHC$_{10}$-900 and NOPHC$_{10}$-H$_{24}$ as the same material, prepared with 0.10 g of Co_2P template, pyrolyzed at 900 °C, and treated with HCl for 24 h. In addition, for comparison, two control materials, NOPCB and NOCB, were also synthesized at the optimal pyrolysis temperature of 900 °C without including Co_2P templates.

X-ray diffraction (XRD) patterns (Fig. 2a and S1) revealed that all the NOPHCs possessed only two broad diffraction peaks at *ca.* 26.0 ° and 43.5 °, which can be assigned to the (002) and (101) lattice planes of graphite-2H (PDF#41-1487), respectively. However, the XRD patterns of $Co_2P@NOPC$ materials, before treatment with HCl solution, showed several diffraction peaks associated with crystalline Co_2P (PDF#32-0306) along with the graphite-2H. As the $Co_2P@NOPC$ materials were increasingly etched with HCl solution, the peaks related to Co_2P gradually disappeared, leaving only the two characteristic carbon peaks, as seen in the XRD patterns of NOPHC$_{10}$-H$_{24}$ and NOPHC$_{10}$-H$_{48}$. This suggests the complete removal of Co_2P nanoparticles (templates) after treatment in HCl solution for 24 h. Meanwhile, the two distinct carbon peaks were also observed in the XRD patterns of the two control materials NOPCB and NOCB (Fig. S1d). Energy dispersive X-ray spectroscopy (EDX) of NOPHC$_{10}$-900 (Fig. 2b) revealed the presence of C, N, O and P elements, with no detectable Co element.

Scanning electron microscope (SEM) image is displayed in Fig. 2c. It showed that NOPHC$_{10}$-900 (*i.e.* NOPHC$_{10}$-H$_{24}$) had a hollow sphere-like structure. On the other hand, $Co_2P@NOPC$ (Fig. S2a,b) possessed a solid interconnected particles morphology with diameters of 100–200 nm with no hollow one as NOPHC$_{10}$-900 did. These results suggest that the hollow structure in the former must have resulted from the dissolution of Co_2P nanoparticles in HCl solution. Meanwhile the corresponding image of NOPHC$_{10}$-H$_{12}$ material showed both solid and hollow particles (Fig. S2c,d and S3a,b), corroborating the gradual disappearance of Co_2P templates, in line with the XRD results discussed earlier. When the etching time was increased from 24 to 48 h, most of the hollow spheres collapsed (Fig. S2e-h), resulting from the deficient
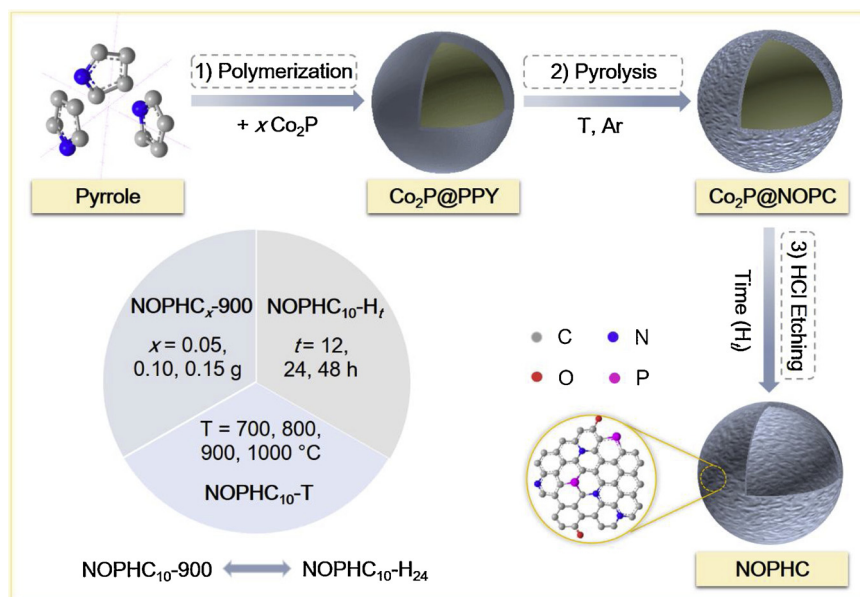

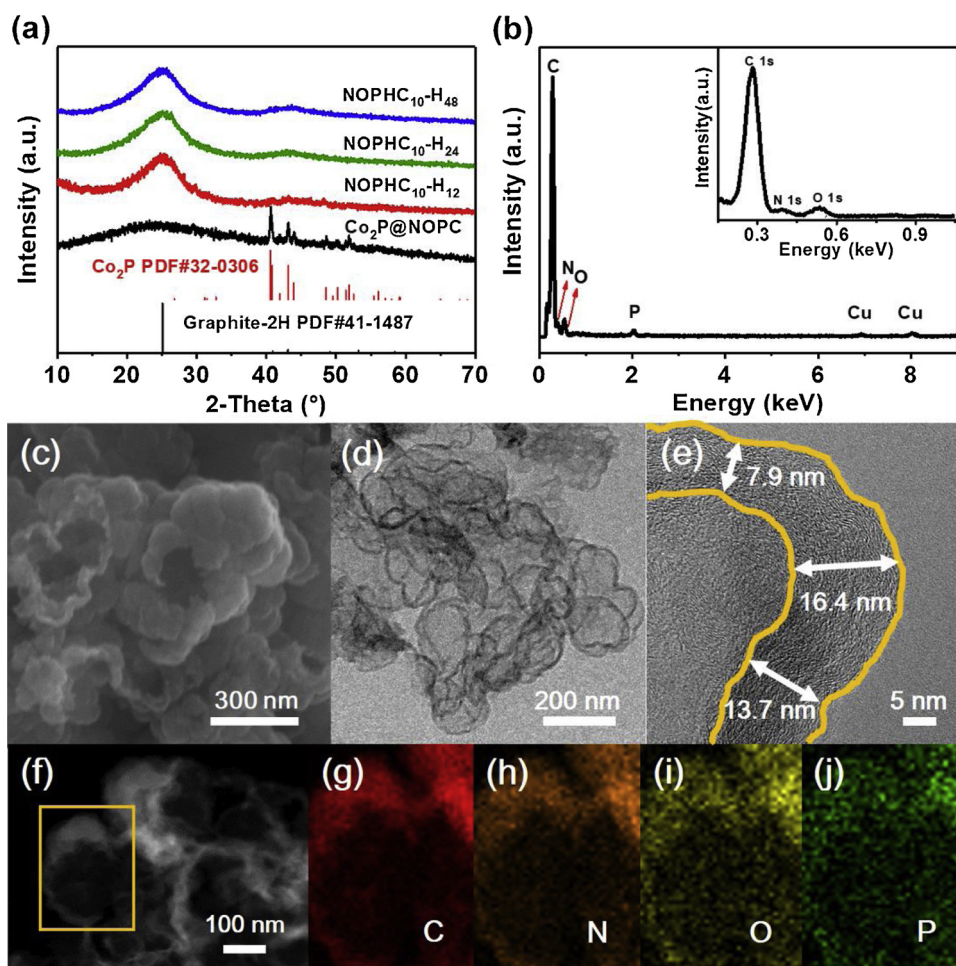**Fig. 1.** Synthetic procedure used to prepare NOPHCs electrocatalysts.

Fig. 2. a) XRD patterns of Co$_2$P@NOPC and NOPHC$_{10}$-H$_t$. Characterization of NOPHC$_{10}$-900 (*i.e.* NOPHC$_{10}$-H$_{24}$): b) EDX spectrum, c) SEM image, d) TEM image, e) HRTEM image, f) HAADF image and g-j) the elemental mapping images from the marked yellow square in f) (For interpretation of the references to colour in this figure legend, the reader is referred to the web version of this article).

rigidity of polymer-derived carbon shells to resist excessive stirring and contraction stress [33,34]. This indicates the successful use of the Co$_2$P nanoparticles as templates and how the subsequent etching time in HCl solution slowly leads to carbon nanomaterials with hollow features. Transmission electron microscope (TEM) and high-resolution TEM (HRTEM) images of NOPHC$_{10}$-900 (Fig. 2d, e and S3c–h) displayed the hollow structure was present uniformly in the material, and the thickness of carbon shell ranged from *ca.* 7.9 to 18.9 nm with multiple graphitic layers. The hollow feature is expected to create more accessible catalytically active sites on the materials that can easily contact electrolytes during electrochemical reactions. Elemental mapping, taken from the marked region in the high angle annular dark field (HAADF) image (Fig. 2f–j), showed an even distribution of C as well as the heteroatom dopant elements (N, O, and P) throughout the as-synthesized carbon material. However, both of the control materials of NOCB and NOPCB, prepared without using Co$_2$P template, exhibited onion-like interconnected structures with no hollow features (Fig. S4).

X-ray photoelectron spectroscopy (XPS) was carried out to verify the surface compositions and the chemical states of the elements. The main peaks located at the binding energies of 284.8, 401.0 and 532.2 eV in survey XPS spectra of NOPHC$_{10}$-T and NOPHC$_x$-900 (Fig. 3a and S5) were ascribed to C 1s, N 1s and O 1s, respectively [35]. The N dopant atoms must have come from the decomposition of PPY precursor during pyrolysis process. And the O atoms must have come from the oxygen-containing groups absorbed on the materials (hydroxyl and carboxyl groups) and/or the oxygen atoms doped into the carbon framework, which were interpreted by the O1s deconvoluted peaks below. The

weak peak centered at 132.8 eV was indexed to P 2p dopant atoms, which must have come from the decomposition of Co$_2$P nanoparticles and their subsequent incorporation into the carbon material. In accordance with the EDX results discussed earlier, there were no peaks associated with Co 2p in these materials, further indicating the Co species associated with Co$_2$P or Co nanoparticles were thoroughly removed, making these materials metal-free. With increasing the pyrolysis temperature from 700 to 1000 °C, the atomic ratio of N:C gradually decreased (from 14.0 to 6.6 %), while the P:C atomic ratio showed the opposite trend (increasing from 0.4 to 2.0 %), as shown in Fig. 3b and Table S2. These might be because, as higher pyrolysis temperature was applied, more N atoms were lost but relatively more P atoms were decomposed from Co$_2$P and then made it into the carbon material, which are in agreement with previous reports [31,36].

The high-resolution XPS spectra of C 1s in NOPHC$_{10}$-T and NOPHC$_x$-900 (Fig. S6-8) displayed all the C 1s peaks in NOPHCs could be further deconvoluted into five peaks, corresponding to C=C−C (284.8 eV), C−P (285.2 eV), C−O/C−N (286.1 eV), C(=O)−O (288.0 eV) and π-π* (290.5 eV) moieties [37,38]. The presence of the peaks corresponding to C−P and C−N species in the deconvoluted spectra of C 1s confirmed that N and P atoms were successfully doped into the NOPHCs. Note that there were no peaks related to C−P bond in the control material NOCB (Fig. S9a). In the case of the high-resolution XPS spectra of N 1s (Fig. S10-S13), two main peaks associated with pyridinic-N (398.4 eV) and graphitic-N (401.0 eV) species were observed, both of which were reported to be active catalytic sites for ORR [39]. As can be seen in Fig. S14, higher pyrolysis temperature led to a
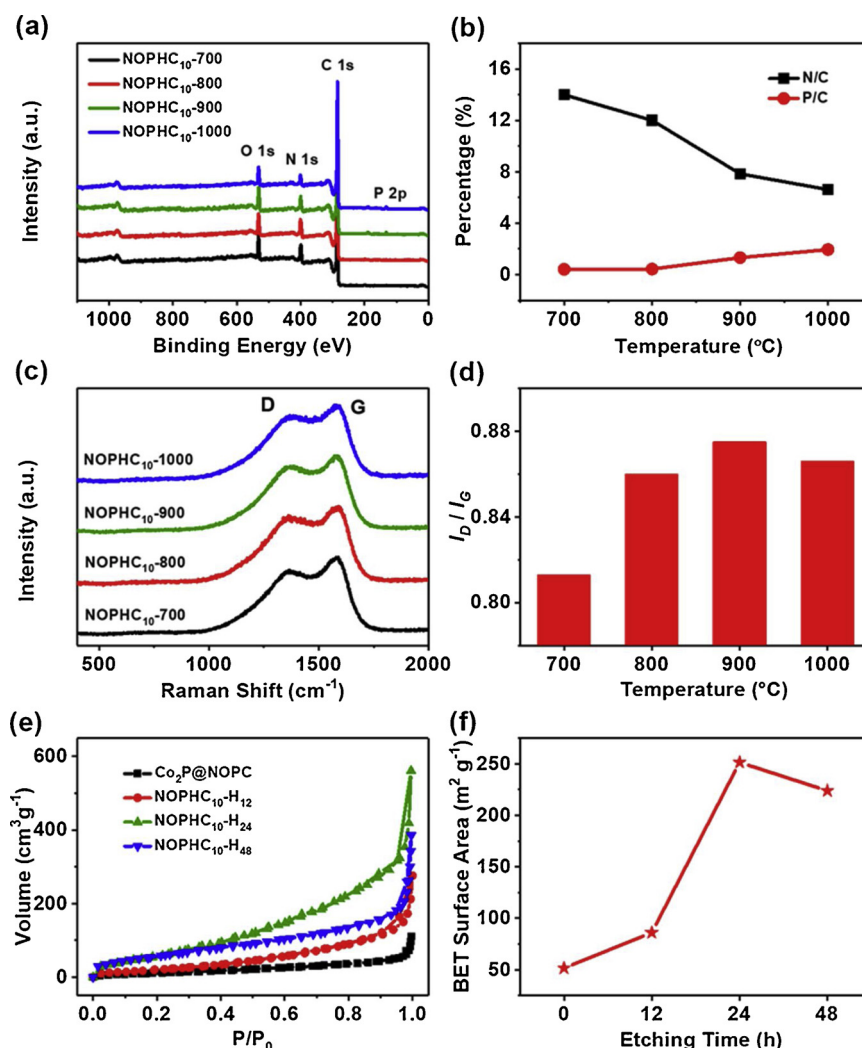
Fig. 3. a) XPS survey spectra of NOPHC$_{10}$-T, b) the tendency curves of N/C and P/C as a function of pyrolysis temperature, c) Raman spectra of NOPHC$_{10}$-T, d) the ratio of I_D/I_G over NOPHC$_{10}$-T, e) N$_2$ adsorption/desorption isotherms of Co$_2$P@NOPC and NOPHC$_{10}$-H$_t$, and f) the BET surface area of Co$_2$P@NOPC and NOPHC$_{10}$-H$_t$.

significant increase in the amount of graphitic-N and a decrease in the amount of pyridinic-N, which might be caused by the conversion of less stable pyridinic-N into graphitic-N when higher temperature employed [40]. Notably, graphitic-N were more prevalent than pyridinic-N in the whole temperature range of 700-1000 °C (65-85 %). There were three peaks in the O 1s deconvoluted spectra of NOPHC$_{10}$-900, NOCB and NOPCB materials (Fig. S15a). The two peaks centered at 532.0, 533.3 eV belonged to surface hydroxyl and carboxyl groups, respectively [41]. Besides the peak at 530.5 eV was related with C−O species in the carbon lattice [42], giving the evidence for successful doping of oxygen atoms into the carbon skeleton. As shown in Fig. S15b, resulting from the presence of P dopants, the content of intracell C−O species in NOPHC$_{10}$-900 and NOPCB were markedly higher than those in NOCB. Regarding to the deconvoluted P 2p spectra (Fig. S16 and S17), two peaks at 132.8 and 134.3 eV associated with P−C and PO$_4^{3-}$ species, respectively, were observed [43], confirming these materials were Co$_2$P-free. Notably, the small amount of PO$_4^{3-}$ species probably resulted from partially oxidized surface under air. However, a Co 2p peak was present along with the C 1s, N 1s, O 1s and P 2p peaks in the survey spectrum of Co$_2$P@NOPC (Fig. S5b), which suggests the presence of Co$_2$P. In contrast to the materials of NOPHC$_{10}$-H$_{24}$ and NOPHC$_{10}$-H$_{48}$, two additional P-Co characteristic peaks (129.9 eV, 130.7 eV) [44] also showed up along with a strong peak of P−C bond in the deconvoluted P 2p spectrum for NOPHC$_{10}$-H$_{12}$ material (Fig. S18b), indicating the

existence of a small amount of Co$_2$P in NOPHC$_{10}$-H$_{12}$ and the beneficial feature of longer etching time in the formation of metal-free carbon materials. In the control sample of NOPCB, only two peaks corresponding to P−C and PO$_4^{3-}$ in P 2p deconvoluted XPS spectrum were seen (Fig. S19).

Raman spectra presented two distinct carbon peaks: a D band at 1365 cm^{-1}, which is generally related to the disordered structures/structural defects in carbon materials, and a G band at 1580 cm^{-1} associated with the in-plane stretching vibration of graphitic carbon atoms (Fig. 3c and S20) [45,46]. The D band goes in line with the presence of N, O and P dopants and the concomitant absence of some carbon atoms in the carbon lattice. The ratio of I_D/I_G, displayed in Fig. 3d, which reflects the relative degree of disordered to ordered carbon structure in the material, increased from 0.813 to 0.875 as the pyrolysis temperature was raised from 700 to 900 °C, and then decreased to 0.866 when the temperature was 1000 °C. So, among the materials, the one synthesized at pyrolysis temperature of 900 °C had the highest I_D/I_G ratio. The first increase is the result of giving more dopants and structural defects, caused by decomposition of Co$_2$P and P doping into the carbon matrix as the pyrolysis temperature increases, and the subsequent decrease can be attributed to the severe decomposition of in-plane heteroatoms at 1000 °C [47]. Besides, the increase in the amount of Co$_2$P allowed the I_D/I_G ratio first to increase and then to decrease (Fig. S20a,b). The Co and P, stemmed from decomposition

of Co_2P, were favorable for graphitization and the formation of structural defects, respectively, in the carbon materials. It appeared that P doping was relatively favored when the amount of Co_2P template was small, while graphitization by Co was relatively dominated when more Co_2P was used. Moreover, the ratio of I_D/I_G increased slightly when the acidic treatment time was increased (Fig. S20c,d), most likely because more edges along with more defect sites were exposed when longer etching time was employed and sacrificial Co_2P templates were removed. Meanwhile, the control sample NOPCB had a relatively higher I_D/I_G ratio than NOCB (Fig. S20e,f), which was because more P dopant atoms were introduced in carbon framework increasing the intensity of D band.

N_2 adsorption/desorption isotherms (Fig. 3e and S21) exhibited that all the materials possessed Type IV isotherms with hysteresis loops. As the acidic treatment time was increased, the Brunauer-Emmett-Teller (BET) surface area of the materials gradually increased (for example, to $251\,m^2\,g^{-1}$ for $NOPHC_{10}$-H_{24}, compared with $52\,m^2\,g^{-1}$ for $Co_2P@$ NOPC) (Fig. 3f). This might be because as more Co_2P templates were removed by the acid treatment, larger exposed carbon surfaces were formed. It was worth noting that the surface area in $NOPHC_{10}$-H_{24} was nearly five times higher than that of its parent material $Co_2P@NOPC$, and expected to expose more catalytic active sites and facilitate faster electrochemical processes. However, further treatment with acidic solution made the hollow structure partially collapsed and the BET surface area slightly decreased. Moreover, in the case of the series of $NOPHC_x$-900 materials, when the amount of Co_2P was increased, the BET surface area of the materials first increased evidently but then slightly reduced, giving $NOPHC_{10}$-900 had the largest value (Fig. S22). As more well-dispersed Co_2P templates could promote the formation of more carbon-embedded Co_2P particles, larger amount of hollow structures can be formed in $NOPHC_{10}$-900 than that in $NOPHC_5$-900, leading to a substantial increase in BET surface area over $NOPHC_{10}$-900. On the contrary, surplus Co_2P templates used for producing $Co_2P@PPY$ precursors easily suffered from agglomeration and poor dispersion in the solution, which might bring less encapsulated structures and give lower BET surface area compared to that of $NOPHC_{10}$-900 [48].

3.2. Electrocatalytic activities towards HER and ORR

The electrocatalytic activities toward HER of all the synthesized materials were then measured on a standard three-electrode system. As a comparison, the catalytic activity of a commercially available Pt/C (20 *wt.* %) was also evaluated under otherwise the same condition. All the LSVs were acquired in 1.0 M KOH solution and shown without *iR*-compensation unless mentioned otherwise. As can be seen in Fig. 4a and S23, $NOPHC_{10}$-900 (*i.e.*, $NOPHC_{10}$-H_{24}) exhibited remarkable electrocatalytic activity, with a small onset potential of 180 mV *versus* the reversible hydrogen electrode (RHE) and a small overpotential of 290 mV to produce a current density of $10\,mA\,cm^{-2}$. Although its activity cannot be comparable with that of commercial Pt/C (20 *wt.* %) electrocatalyst (Fig. S23), it is comparable with those of some of the most efficient metal-free alkaline HER electrocatalysts recently reported (see Table S3). After *iR*-correction, $NOPHC_{10}$-900's current densities were 10 and $20\,mA\,cm^{-2}$ at overpotentials of *ca.* 280 and 315 mV, respectively (Fig. S24). Both the control materials NOCB and NOPCB also electrocatalyzed HER under identical condition, but they exhibited inferior activities compared with NOPHCs. Although both of them had similar surface area, NOPCB displayed a slightly better electrocatalytic activity than that of NOCB toward HER; this indicated that the P dopant involved in the carbon structure played a significant role in promoting the former's electrocatalytic activity. In fact, P dopant atoms has been reported to be able to adjust the electron density and decrease the work function of the neighbor carbon atoms in carbon materials [27].

Although all the NOPHC materials showed better activity than both NOCB and NOPCB, there were differences among them. The $NOPHC_5$-

900 and $NOPHC_{15}$-900 materials (obtained with 0.05 and 0.15 g of Co_2P template, respectively) afforded much more negative onset potentials and smaller current densities than $NOPHC_{10}$-900 (obtained with 0.10 g of Co_2P template) (see all electrochemical performance results compiled in Table S4). $NOPHC_{10}$-900's higher electrocatalytic activity toward HER compared with $NOPHC_5$-900 and $NOPHC_{15}$-900 materials must have been due to the larger surface area and more accessible active sites present in the former material. In the case of the series of $NOPHC_{10}$-H_t materials, although $Co_2P@NOPC$ and $NOPHC_{10}$-H_{12} was able to electrocatalyze HER with better activities compared with $NOHPC_{10}$-H_{24} ($NOPHC_{10}$-900), $NOPHC_{10}$-H_{24} endowed remarkable stability (Fig. 4b and S24b). There was barely any current density loss over $NOPHC_{10}$-H_{24} after 19 h long continuous electrochemical HER, and the LSV curve after stability reaction almost overlapped the initial one (the inset in Fig. 4b). Whereas, $Co_2P@NOPC$ exhibited 45% loss of catalytic activity even after 5 h. The poor stability of $Co_2P@$ NOPC might be due to the gradual dissolution of P and the formation of cobalt hydroxide on the surface of Co_2P during the HER process in the alkaline media [49]. As can be seen from the SEM and TEM images in Fig. S25, the material after long-term HER operation presented hollow structures as the original ones, without any collapse or broken, illustrating a remarkable structural stability of $NOPHC_{10}$-900. Besides, XPS results (Fig. S26) demonstrated there were no obvious difference in the peaks related to Graphitic-N and Pyridinic-N, as well as major P-C and minor PO_4^{3-} species in comparison with the original ones before electrocatalytic reactions, giving a good compositional stability. $NOPHC_{10}$-H_{48}, which was treated with HCl solution for 48 h, showed lower catalytic activity with respect to $NOPHC_{10}$-H_{24}. Since Table S2 and Fig. S19 exhibited fairly resemblance in the elements composition and graphitization degree between $NOPHC_{10}$-H_{24} and $NOPHC_{10}$-H_{48}, the inferior performance of $NOPHC_{10}$-H_{48} was most likely because of the partial collapse of hollow sphere along with small BET surface area. Based on the above results, the hollow structure and large BET surface area are favorable for the contact of reactants/intermediates (*i.e.*, H_2O and H^*) with the materials and endow many accessible active sites on the surface, both of which lead to good electrocatalytic activities. Additionally, the electrocatalytic activity by the materials was significantly dependent on the pyrolysis temperature (Fig. S24c). Upon increasing the pyrolysis temperature from 700 to 900 °C, the activity obviously enhanced with the current density increase and the onset potential shifting to a positive value. Additionally, P doping in N-doped carbon, which was doomed to enhance the charge delocalization and produce more edge sites, was found to rise significantly with pyrolysis temperature elevating (Table S2) [37,50]. Further increasing the pyrolysis temperature to 1000 °C led to the partial destruction of interconnected carbon structure and consequent an increment in charge resistance during reaction (see in EIS of $NOPHC_{10}$-T), giving a decay in electrocatalytic activity [51]. Associated with the largest I_D/I_G in Raman spectra, the best performance of $NOPHC_{10}$-900 might be due to the highest defects in the carbon structure. Furthermore, in comparison with other materials obtained at different pyrolysis temperature, $NOPHC_{10}$-900 presented the highest current density at the same specific overpotential or needed the smallest overpotential to achieve the same given current density. The superior electrocatalytic HER activity over $NOPHC_{10}$-900 catalyst was also supported by the fact that $NOPHC_{10}$-900 possessed the smallest Tafel slope ($102\,mV\,dec^{-1}$) and fastest reaction kinetics among $NOPHC_x$-900 and $NOPHC_{10}$-T materials (Fig. 4c and S27). The Faradaic efficiency of $NOPHC_{10}$-900 toward HER was determined with chronoamperometry over a period of 55 min at an overpotential of 425 mV. The experimentally measured H_2 amount was found to match well with the theoretically expected quantity, indicating $NOPHC_{10}$-900 afforded a ~100 % Faradic yield during HER process in alkaline medium (Fig. 4d).

To gain further insight into the high electrocatalytic activity of NOPHCs, electrochemical impedance spectra (EIS) and electrochemical surface area (ECSA) measurements were carried out. As shown in
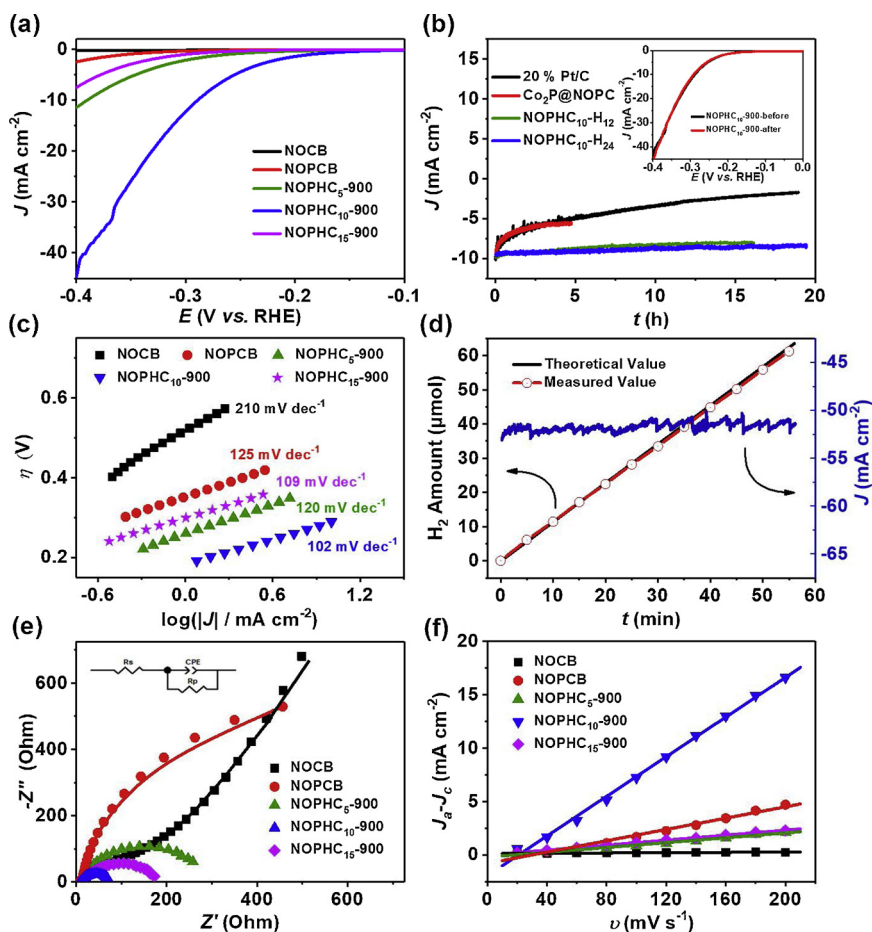
Fig. 4. Electrocatalytic HER peformances over different NOPHCs. a) LSV curves in 1.0 M KOH without *iR*-compensation and b) chronoamperometric curves for $Co_2P@$ NOPC, $NOPHC_{10}$-H_{12} and $NOPHC_{10}$-H_{24}. The insert is the LSV curves of $NOPHC_{10}$-900 ($NOPHC_{10}$-H_{24}) before and after *i-t* test, c) Tafel plots of $NOPHC_x$-900, NOPCB and NOCB electrocatalysts, d) H_2 amount of theoretically calculated and experimentally determined as a function of reaction time over $NOPHC_{10}$-900, e) Nyquist plots and f) electrochemical active surface areas of NOCB, NOPCB and $NOPHC_x$-900. The loading is ~ 0.283 mg cm^{-2}.

Nyquist plots, $NOPHC_{10}$-900 exhibited the smallest radius of semicircle and the smallest charge transfer resistance (R_{ct}) among all the NOPHCs as well as the control samples of $Co_2P@NOPC$, NOPCB and NOCB (Fig. 4e, S28 and Table S4). The remarkable HER performance of $NOPHC_{10}$-900 was mainly attributed to the improved electrical conductivity by heteroatoms doping and the enhanced electron transport rate in electrochemical process. Furthermore, the ECSA value of $NOPHC_{10}$-900 (116.0 cm^2), related with the double-layer capacitance (C_{dl}) and used to evaluate the catalytically active sites, was much larger than those of other NOPHCs synthesized and tested, manifesting $NOPHC_{10}$-900 had more exposed active sites for electrocatalyzing HER (Fig. 4f, S29-30, and Table S4). Based on the results above, we assume that the excellent HER performance over $NOPHC_{10}$-900 metal-free electrocatalyst could be mainly attributed to the following aspects: i) The graphitic carbon shells possess good intrinsic electronic conductivity, facilitating the electron transfer and transport; ii) Heteroatoms (N, O and P) doping in carbon framework can modulate the electronic properties of adjacent carbon, optimizing the adsorption and desorption of intermediates (H*, H_2) on carbon's surface; iii) Multiheteroatoms doping gives a synergetic effect in the enhancement of eletctrocatalytic performance; iv) The hollow structure with large BET surface area is favorable for the electrolyte penetration, endowing the reactants more opportunities to contact the electrocatalysts; and v) The large value of ECSA provides more catalytically active sites on carbon's surface.

Besides serving as remarkable metal-free HER electrocatalysts in alkaline media, the NOPHCs were also found to have good electrocatalytic ORR performance. CVs acquiring at a scan rate of 100 mV s^{-1} for each material were firstly investigated in N$_2$- and O$_2$-saturated 0.1 M KOH electrolyte. There was an obvious redox peak at 0.67 V in the CV profile for the O$_2$-saturated KOH electrolyte, while no response was

observed in the N$_2$-saturated solution over $NOPHC_{10}$-900 electrocatalyst during the same potential range, revealing $NOPHC_{10}$-900 can effectively electrocatalyze ORR in alkaline media (Fig. 5a). LSV was further studied to evaluate the catalytic activity using rotating disk electrode (RDE) technique running at different rotation rates (from 400 to 2025 rpm) in an O$_2$-saturated 0.1 M KOH solution at a sweep rate of 2 mV s^{-1}. The small sweep rate during ORR was able to largely reduce the capacitance effect on the current density. A positive onset and half-wave potential ($E_{1/2}$) of 0.90 and 0.77 V, as well as a large limiting current density of -4.2 mA cm^{-2} were achieved over $NOPHC_{10}$-900 electrode at a rotating speed of 1600 rpm (Fig. 5b and S31), which is comparable with some of efficient metal-free alkaline ORR electrocatalysts reported (Table S5). The Koutecky-Levich (K-L) plots of $NOPHC_{10}$-900 obtained from the LSV curves were found to show good linearity, indicating the ORR exhibited by $NOPHC_{10}$-900 was a first-order kinetic with respect to the dissolved oxygen concentration [52]. The electron transfer number per oxygen molecule (n) in ORR, based on the slopes of K-L plots, was calculated to be in a range of 3.6–3.7, which suggests it underwent a direct four-electron process over $NOPHC_{10}$-900 (Fig. 5c). Moreover, the value of n, along with the yield of peroxide (H_2O_2 %) in the products, were further examined to explore the catalytic pathways of ORR with rotating ring disk electrode (RRDE) technique. $NOPHC_{10}$-900 provided a low H_2O_2 yield of 15–30 % and a high n value of 3.5–3.6 in a wide potential range of 0.25-0.85 V (*vs.* RHE). In other words, $NOPHC_{10}$-900 had a high selectivity to promote a four-electron reduction process in this potential range and generate H_2O (Fig. S32). However, the control sample NOCB electrocatalyzed ORR with a more negative onset potential (0.77 V). As expected, P doping in the carbon skeleton enables NOPCB material to give a relatively positive onset potential of 0.83 V in ORR. NOPCB's better electrocatalytic activity, once again, confirmed that doping P in the carbon materials
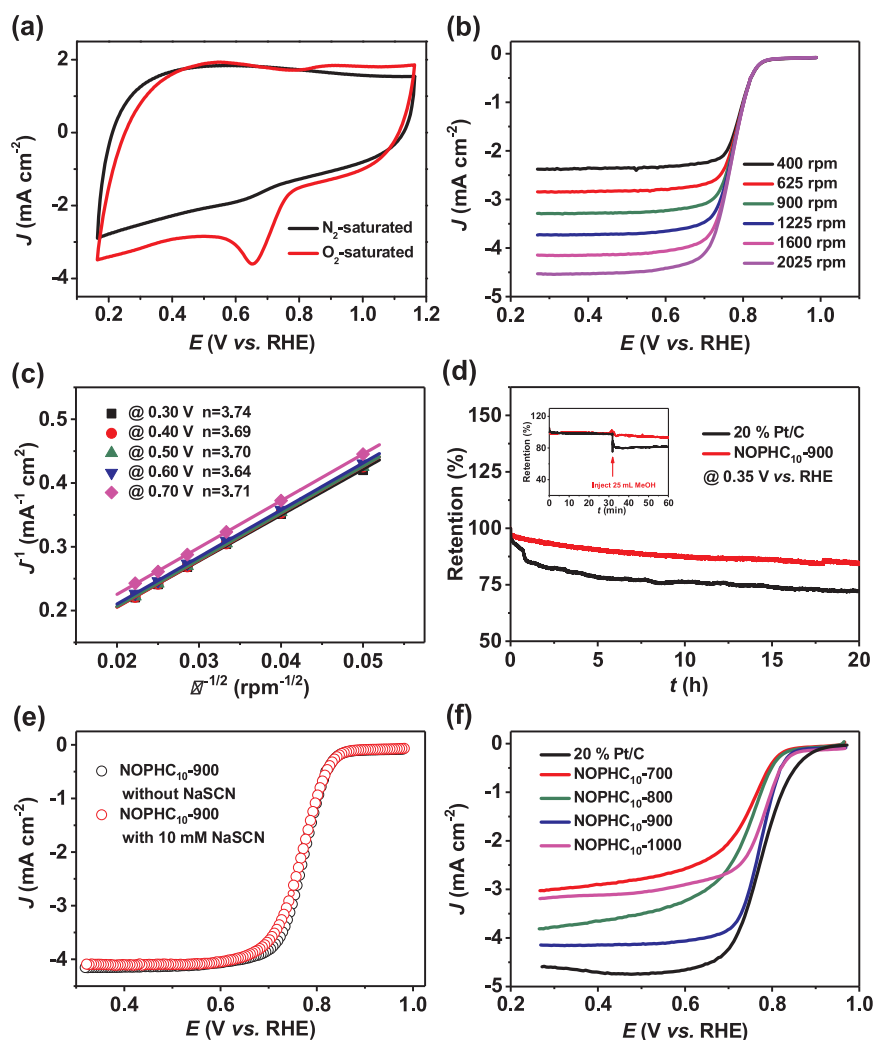
Fig. 5. Electrocatalytic properties toward ORR over different NOPHCs. a) CV scans of NOPHC$_{10}$-900 at a sweep rate of 100 mV s^{-1} in 0.1 M KOH solution, b) LSV curves of NOPHC$_{10}$-900 at a sweep rate of 2 mV s^{-1} on RDE, c) the electron transfer number of NOPHC$_{10}$-900 obtained from corresponding LSV curves, d) chronoamperometric curves and methanol crossover tolerance over NOPHC$_{10}$-900 and commercial Pt/C (20 *wt.* %), e) LSV curves of NOPHC$_{10}$-900 in 0.1 M KOH solution with and without 10 mM NaSCN, and f) LSV curves of NOPHC$_{10}$-T materials on RDE rotating at the speed of 1600 rpm. The loading is ~0.407 mg cm^{-2}.

boosted the material's electrocatalytic activity, due to the modulated electronic structure and the relevant defects.

In addition, chronoamperometric measurement was carried out to assess the stability of NOPHC$_{10}$-900 for ORR at a constant potential of 0.35 V at 1600 rpm (Fig. 5d). For a comparison purpose, the stability of Pt/C (20 *wt.* %) was also conducted in the same way. NOPHC$_{10}$-900 displayed only a slight current loss over 20 h continuous reaction, whereas 20 *wt.* % Pt/C exhibited ~28 % loss of catalytic activity over the same period, which illustrates a good stability of NOPHC$_{10}$-900 for ORR in basic medium. Moreover, the SEM, TEM and XPS characterizations of NOPHC$_{10}$-900 after 20 h ORR (Fig. S33 and S34) demonstrated the morphology and composition did not change after electrocatalytic reaction, suggestion good compositional and structural stability of the electrocatalyst. Methanol crossover test (insert in Fig. 5d) shows that the cathodic ORR current density had no distinct decay after an addition of methanol into the original solution, suggesting its high tolerance for methanol crossover. However, the activity significantly suffered after methanol injection and the methanol oxidation reaction occurred in the case of Pt/C (20 *wt.* %). It is well known that SCN$^-$ ions can strongly coordinate cobalt ions and block the cobalt-centered catalytic sites for ORR [53]. When NOPHC$_{10}$-900 was exposed in the electrolyte containing 10 mM NaSCN, no ORR activity loss was observed comparing the one without NaSCN (Fig. 5e),

suggesting NOPHC$_{10}$-900 is totally Co-species-free. The ORR examination results of other NOPHCs obtained with different pyrolysis temperature, Co$_2$P template amount and acidic etching time were also given. Among all the materials, NOPHC$_{10}$-900 showed the best electrocatalytic performance for ORR, with the most positive onset potential value and largest limiting kinetic current density, smallest Tafel slope and H$_2$O$_2$ yield, as well as close to four electron transfer number (Fig. 5f, S31, S32, S35 and Table S6). This can be ascribed to the lower charge resistance, easier mass transfer property, and more accessible catalytically active sites, which were caused by larger BET surface area and more optimized electronic properties by heteroatoms doping in the carbon structure.

3.3. Density function theory (DFT) calculations

In order to get an in-depth understanding of the catalytic mechanisms over NOPHCs electrocatalysts, density function theory (DFT) calculations were carried out to study the catalytically active sites for HER and ORR processes. According to the XPS results, four molecular models containing pristine graphene (G), graphitic-N doped graphene (N-G), P-doped graphene (P-G) as well as graphitic-N and P dual-doped graphene (N, P-G) were built to investigate the structure-activity relationship (Fig. S36). Note that pyridinic-N doped graphene model was
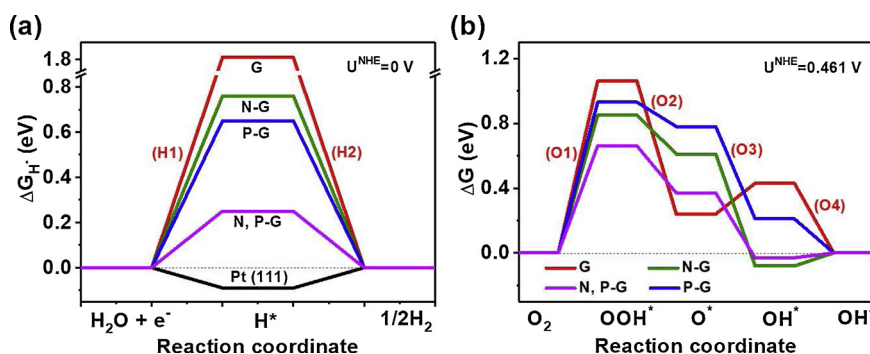
Fig. 6. Gibbs free energy diagram of a) HER and b) ORR in alkaline media. ΔG_H^* of Pt (111) was used as -0.09 eV [50]. The reaction steps inside represent: (H1) $*+ H_2O(l) + e^- \rightarrow H^* + OH^-$, (H2) $H^* + H_2O(l) + e^- \rightarrow *+ H_2(g) + OH^-$, (O1) $*+ O_2(g) + H_2O(l) + e^- \rightarrow HOO^* + OH^-$, (O2) $HOO^* + e^- \rightarrow O^* + OH^-$, (O3) $O^* + H_2O(l) + e^- \rightarrow HO^* + OH^-$ and (O4) $HO^* + e^- \rightarrow *+ OH^-$.

not included in this work due to the predominant portion of graphitic-N type over pyridinic-N in the N dopant [54–56]. The calculated band gap of the N, P dual-doped graphene was 0.11 eV and as expected smaller than those of the N or P solely doped graphene (Fig. S37). Therefore, simultaneously doping with N and P can synergistically improve the materials' electrical conductivity and thus enhance the catalytic performance. Besides, differential charge density diagram in Fig. S38 shows the charge delocalization of carbon had been significantly affected by the neighbor N and/or P dopants, inducing the "activation region" on the graphene surface and becoming the active sites to take participate in adsorbing/desorbing H* and OOH* reaction intermediates. Hence, we supposed such carbon atoms were the real active sites to calculate the Gibbs free energy change during HER and ORR process.

It is widely accepted that HER in alkaline solution involves Volmer-Heyrovsky or Volmer-Tafel steps like the case in acidic one, except that the adsorbed hydrogen intermediate (H*) following the Volmer step is generated by an initial water dissociation step ($H_2O + e^- \rightarrow H^* + OH^-$) [57]. Our above experimental results, showing the Tafel slopes of all the NOPHCs around 120 mV dec^{-1}, suggested the HER process over NOPHCs electrocatalysts was a Volmer-Heyrovsky reaction. The strength of hydrogen adsorption on the catalytic surface can be expressed as the Gibbs free energy change for this step (ΔG_H^*). A lower value of $|\Delta G_H^*|$ reflects higher activity for HER. As shown in the HER free energy diagram (Fig. 6a), graphitic carbon in the pristine graphene model exhibited the greatest value of ΔG_H^* (1.82 eV), which was too large to adsorb hydrogen on the catalyst surface. After N and/or P single/dual-doping, the ΔG_H^* remarkably decreased (0.76, 0.65 and 0.25 eV for N-G, P-G and N, P-G, respectively), indicating heteroatoms incorporation was beneficial for strengthening the hydrogen adsorption on graphene and thereby boosting the electrocatalytic activity. Due to the synergistic effect, the N and P dual-doping was expected to make N, P-G material had the smallest ΔG_H^* value and highest activity.

In the case of ORR in basic solution, the N, P co-doped graphene had the lowest overall free energy change (ΔG^*) at the equilibrium potential $U^{SHE} = 0.461$ V and gave the best catalytic activity (Fig. 6b). The first step (O1 in Fig. 6b), where O_2 molecules were absorbed on the active sites and transferred to electrochemically form of OOH*, was uphill and considered to be the rate determining step of the overall reduction reaction. Hence, N and P dopants can largely reduce the activation barrier of ORR on the carbon surface, especially in the most sluggish step (*i.e.* O_2 adsorption step, O1). According to the above results, we conclude that N and P doping, especially for the simultaneous doping, in the carbon framework is an effective way to change the work function by modulating its electronic properties and create active defect sites, and thereby improve the electrocatalytic activity.

4. Conclusions

In summary, N-, O- and P-doped hollow carbons have been successfully synthesized by pyrolysis of Co_2P-containing PPY precursors and removal of Co_2P sacrificial templates. These metal-free materials have been shown to serve as highly stable, bifunctional electrocatlysts for both HER and ORR in alkaline media. Notably, NOPHC$_{10}$-900 has been found to deliver a current density of -10 mA cm^{-2} at small overpotential of 290 mV, along with giving remarkable stability of 19 h and high quantitative Faradic efficiency of ~100 % for the HER. Moreover, NOPHC$_{10}$-900 has been found to catalyze ORR with quite positive onset potential of 0.90 V (low overpotential), good methanol crossover tolerance and outstanding durability for at least 20 h. The remarkable electrocatalytic properties are mainly owning to the hollow structure with high density of electrocatalytically active sites and heteroatoms doping with enhanced conductivity and optimized charge delocalization. We strongly believe this work will open up a way to develop advanced and highly active bifunctional metal-free catalysts for both HER and ORR.

Appendix A. Supplementary data

Supplementary material related to this article can be found, in the online version, at doi:https://doi.org/10.1016/j.apcatb.2019.01.080.

References

[1] M.S. Dresselhaus, I.L. Thomas, Nature 414 (2001) 332–337.
[2] H.B. Gray, Nat. Chem. 1 (2009) 7–8.
[3] M.G. Walter, E.L. Warren, J.R. McKone, S.W. Boettcher, Q. Mi, E.A. Santori, N.S. Lewis, Chem. Rev. 110 (2010) 6446–6473.
[4] Z. Fan, Z. Luo, X. Huang, B. Li, Y. Chen, J. Wang, Y. Hu, H. Zhang, J. Am. Chem. Soc. 138 (2016) 1414–1419.
[5] J. Greeley, T.F. Jaramillo, J. Bonde, I. Chorkendorff, J.K. Nørskov, Nat. Mater. 5 (2006) 909–913.
[6] B. Hinnemann, P.G. Moses, J. Bonde, K.P. Jørgensen, J.H. Nielsen, S. Horch, I. Chorkendorff, J.K. Nørskov, J. Am. Chem. Soc. 127 (2005) 5308–5309.

[7] M.A. Lukowski, A.S. Daniel, F. Meng, A. Forticaux, L. Li, S. Jin, J. Am. Chem. Soc. 135 (2013) 10274–10277.

[8] Y. Li, K. Yin, L. Wang, X. Lu, Y. Zhang, Y. Liu, D. Yan, Y. Son, S. Luo, Appl. Catal. B-Environ. 239 (2018) 537–544.

[9] S. Gupta, N. Patel, R. Fernandes, R. Kadrekar, A. Dashora, A.K. Yadav, D. Bhattacharyya, S.N. Jha, A. Miotello, D.C. Kothari, Appl. Catal. B-Environ. 192 (2016) 126–133.

[10] X. Ma, J. Wen, S. Zhang, H. Yuan, K. Li, F. Yan, X. Zhang, Y. Chen, ACS Sustainable Chem. Eng. 5 (2017) 10266–10274.

[11] S.K. Kim, Y. Qiu, Y.-J. Zhang, R. Hurt, A. Peterson, Appl. Catal. B-Environ. 235 (2018) 36–44.

[12] S. Emin, C. Altinkaya, A. Semerci, H. Okuyucu, A. Yildiz, P. Stefanov, Appl. Catal. B-Environ. 236 (2018) 147–153.

[13] K. Zhang, Y. Zhao, D. Fu, Y. Chen, J. Mater. Chem. A 3 (2015) 5783–5788.

[14] D. Kong, H. Wang, J.J. Cha, M. Pasta, K.J. Koski, J. Yao, Y. Cui, Nano Lett. 13 (2013) 1341–1347.

[15] M. Shalom, D. Ressnig, X. Yang, G. Clavel, T.P. Fellinger, M. Antonietti, J. Mater. Chem. A 3 (2015) 8171–8177.

[16] Z. Yin, Y. Sun, C. Zhu, C. Li, X. Zhang, Y. Chen, J. Mater. Chem. A 5 (2017) 13648–13658.

[17] Y. Wang, Y. Sun, F. Yan, C. Zhu, P. Gao, X. Zhang, Y. Chen, J. Mater. Chem. A 6 (2018) 8479–8487.

[18] Z. Pu, S. Wei, Z. Chen, S. Mu, Appl. Catal. B-Environ. 196 (2016) 193–198.

[19] X. Yu, S. Zhang, C. Li, C. Zhu, Y. Chen, P. Gao, L. Qi, X. Zhang, Nanoscale 8 (2016) 10902–10907.

[20] Z. Yin, C. Zhu, C. Li, S. Zhang, X. Zhang, Y. Chen, Nanoscale 8 (2016) 19129–19138.

[21] L. Zhang, Y. Yang, M.A. Ziaee, K. Lu, R. Wang, ACS Appl. Mater. Interfaces 10 (2018) 9460–9467.

[22] J. Deng, P. Ren, D. Deng, X. Bao, Angew. Chem. Int. Ed. 54 (2015) 2100–2104.

[23] Y. Cao, Y. Meng, S. Huang, S. He, X. Li, S. Tong, M. Wu, ACS Sustainable Chem. Eng. 6 (2018) 15582–15590.

[24] M. Tavakkoli, T. Kallio, O. Reynaud, A.G. Nasibulin, C. Johans, J. Sainio, H. Jiang, E.I. Kauppinen, K. Laasonen, Angew. Chem. Int. Ed. 54 (2015) 4535–4538.

[25] J. Wang, D. Gao, G. Wang, S. Miao, H. Wu, J. Li, X. Bao, J. Mater. Chem. A 2 (2014) 20067–20074.

[26] J.P. Paraknowitsch, A. Thomas, Energy Environ. Sci. 6 (2013) 2839–2855.

[27] Y. Zheng, Y. Jiao, L. Li, T. Xing, Y. Chen, M. Jaroniec, S.Z. Qiao, ACS Nano 8 (2014) 5290–5296.

[28] Y. Ito, W. Cong, T. Fujita, Z. Tang, M. Chen, Angew. Chem. Int. Ed. 54 (2015) 2131–2136.

[29] K. Gong, F. Du, Z. Xia, M. Durstock, L. Dai, Science 323 (2009) 760–764.

[30] L. Yu, H.B. Wu, X.W. Lou, Acc. Chem. Res. 50 (2017) 293–301.

[31] S. Huang, Y. Meng, S. He, A. Goswami, Q. Wu, J. Li, S. Tong, T. Asefa, M. Wu, Adv. Funct. Mater. 27 (2017) 1606585.

[32] Y. Meng, D. Voiry, A. Goswami, X. Zou, X. Huang, M. Chhowalla, Z. Liu, T. Asefa, J. Am. Chem. Soc. 136 (2014) 13554–13557.

[33] X.W. Lou, C.M. Li, L.A. Archer, Adv. Mater. 21 (2009) 2536–2539.

[34] S. Yang, X. Feng, L. Zhi, Q. Cao, J. Maier, K. Müllen, Adv. Mater. 22 (2010) 838–842.

[35] S. Chen, J. Bi, Y. Zhao, L. Yang, C. Zhang, Y. Ma, Q. Wu, X. Wang, Z. Hu, Adv. Mater. 24 (2012) 5593–5597.

[36] L. Lin, Q. Zhu, A. Xu, J. Am. Chem. Soc. 136 (2014) 11027–11033.

[37] R. Li, Z. Wei, X. Gou, ACS Catal. 5 (2015) 4133–4142.

[38] X. Yu, S. Zhang, C. Li, C. Zhu, Y. Chen, P. Gao, L. Qi, X. Zhang, Nanoscale 8 (2016) 10902–10907.

[39] H. Wu, J. Geng, H. Ge, Z. Guo, Y. Wang, G. Zheng, Adv. Energy Mater. 6 (2016) 1600794.

[40] T. Sharifi, G. Hu, X. Jia, T. Wågberg, ACS Nano 6 (2012) 8904–8912.

[41] J. Fu, B. Zhu, C. Jiang, B. Cheng, W. You, J. Yu, Small 13 (2017) 1603938.

[42] J. Duan, S. Chen, B.A. Chambers, G.G. Andersson, S.Z. Qiao, Adv. Mater. 27 (2015) 4234–4241.

[43] J. Yang, H. Sun, H. Liang, H. Ji, L. Song, C. Gao, H. Xu, Adv. Mater. 28 (2016) 4606–4613.

[44] M. Zhuang, X. Ou, Y. Dou, L. Zhang, Q. Zhang, R. Wu, Y. Ding, M. Shao, Z. Luo, Nano Lett. 16 (2016) 4691–4698.

[45] H. Zhang, Z. Ma, J. Duan, H. Liu, G. Liu, T. Wang, K. Chang, M. Li, L. Shi, X. Meng, K. Wu, J. Ye, ACS Nano 10 (2016) 684–694.

[46] A.C. Ferrari, D.M. Basko, Nat. Nanotechnology 8 (2013) 235–246.

[47] A. Mulyadi, Z. Zhang, M. Dutzer, W. Liu, Y. Deng, Nano Energy 32 (2017) 336–346.

[48] Z. Xing, M. Xiao, Z. Guo, W. Yang, Chem. Commun. 54 (2018) 4017–4020.

[49] Y. Zhang, L. Gao, E.J.M. Hensen, J.P. Hofmann, ACS Energy Lett. 3 (2018) 1360–1365.

[50] C.H. Choi, S.H. Park, S.I. Woo, ACS Nano 6 (2012) 7084–7091.

[51] C.H. Choi, S.H. Park, S.I. Woo, J. Mater. Chem. 22 (2012) 12107–12115.

[52] H.X. Zhong, J. Wang, Y.W. Zhang, W.L. Xu, W. Xing, D. Xu, Y.F. Zhang, X.B. Zhang, Angew. Chem. Int. Ed. 53 (2014) 14235–14239.

[53] I.S. Amiinu, X. Liu, Z. Pu, W. Li, Q. Li, J. Zhang, H. Tang, H. Zhang, S. Mu, Adv. Funct. Mater. 28 (2018) 1704638.

[54] Y. Jiao, Y. Zheng, K. Davey, S. Qiao, Nat. Energy 1 (2016) 16130–16138.

[55] K. Qu, Y. Zheng, X. Zhang, K. Davey, S. Dai, S. Qiao, ACS Nano 11 (2017) 7293–7300.

[56] Y. Zheng, Y. Jiao, S. Qiao, Adv. Mater. 27 (2015) 5372–5378.

[57] J.K. Nørskov, T. Bligaard, A. Logadottir, J.R. Kitchin, J.G. Chen, S. Pandelov, U. Stimming, J. Electrochem. Soc. 152 (2005) J23–J26.